Two-Nanometer Voids in Single-Layer Hexagonal Boron Nitride: Formation *via* the "Can-Opener" Effect and Annihilation by Self-Healing

Huanyao Cun,[†] Marcella Iannuzzi,[‡] Adrian Hemmi,[†] Jürg Osterwalder,[†] and Thomas Greber[†,*]

[†]Physik-Institut, Universität Zürich, Winterthurerstrasse 190, CH-8057 Zürich, Switzerland and [‡]Physikalisch-Chemisches Institut, Universität Zürich, Winterthurerstrasse 190, CH-8057 Zürich, Switzerland

ABSTRACT The exposure of hexagonal boron nitride single layers to low energy ions leads to the formation of vacancy defects that are mobile at elevated temperatures. For the case of *h*-BN on rhodium, a superhoneycomb surface with 3 nm lattice constant (nanomesh), a concerted self-assembly of these defects is observed, where the "can-opener" effect leads to the cut-out of 2 nm "lids" and stable voids in the *h*-BN layer. These clean-cut voids repel each other, which enables the formation of arrays with a nearest neighbor distance down to about 8 nm. The density of voids depends on the Ar ion dose, and can reach 10^{12} cm^{-2}. If the structures are annealed above 1000 K, the voids disappear and pristine *h*-BN nanomesh with larger holes is recovered. The results are obtained by scanning tunneling microscopy and density functional theory calculations.

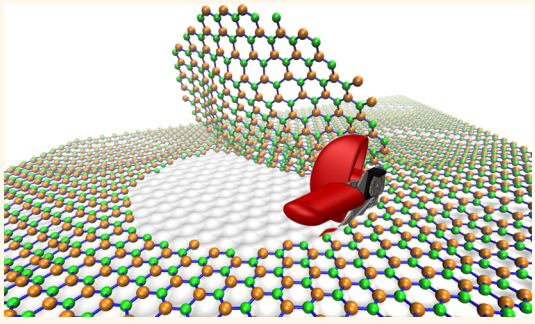

KEYWORDS: hexagonal boron nitride · defect · nanotent · "can-opener" effect · self-healing

Graphene[1] and hexagonal boron nitride (*h*-BN)[2] monolayers have been in the research spotlight since the discoveries of their fascinating properties, such as high mechanical strength, transparency, good thermal conductivity or excellent chemical and thermal stability. Electronically they are complementary: While graphene has a high carrier mobility and is a zero band gap semiconductor, hexagonal boron nitride is a wide band gap insulator with optoelectronic promises.[3,4] Importantly, such sp^2 monolayers formed by chemical vapor deposition (CVD) or segregation processes on a variety of substrates[5−12] exhibit superstructures with a few nanometers lattice constants. They have also been studied and used in view of molecular self-assembly,[6,13,14] charge transfer[11,15] and intercalation.[7,16−19] The functionalization of the sp^2 layers is a major topic in materials science.[20] Beyond chemical approaches,[21] it was realized that also defects created by ion irradiation induce new functionalities,[22,23] or ways to pattern new nanostructures.[24−26]

The *h*-BN monolayer on Rh(111), the so-called nanomesh,[5] is a corrugated honeycomb superstructure formed by high-temperature CVD of borazine $(HBNH)_3$ precursor molecules.[20] The highly regular corrugated structure with a periodicity of 3.2 nm is determined by the mismatch between the boron nitride and the Rh. The unit cell of the *h*-BN nanomesh consists of 13 × 13 BN units on 12 × 12 Rh atoms. The *h*-BN nanomesh unit cell has one "pore" with 2 nm diameter, where the BN is closely attached to the substrate, and is surrounded by "wire"-regions with weak bonding to the substrate and a larger layer-substrate distance.[20,27]

In previous work we reported the formation of Ar and Rb nanotents by the exposure of the *h*-BN nanomesh to low energy ions.[24,28] The immobilization of atoms occurs at two distinct sites beneath the "wire crossings" of the *h*-BN nanomesh superhoneycomb. It was found that the implantation length (*i.e.*, the distance that Ar atoms move after penetration beneath the *h*-BN monolayer before they localize in nanotents) is about 8 nm and the occupation

* Address correspondence to greber@physik.uzh.ch.

Received for review May 14, 2014 and accepted June 16, 2014.

Published online June 17, 2014
10.1021/nn502645w

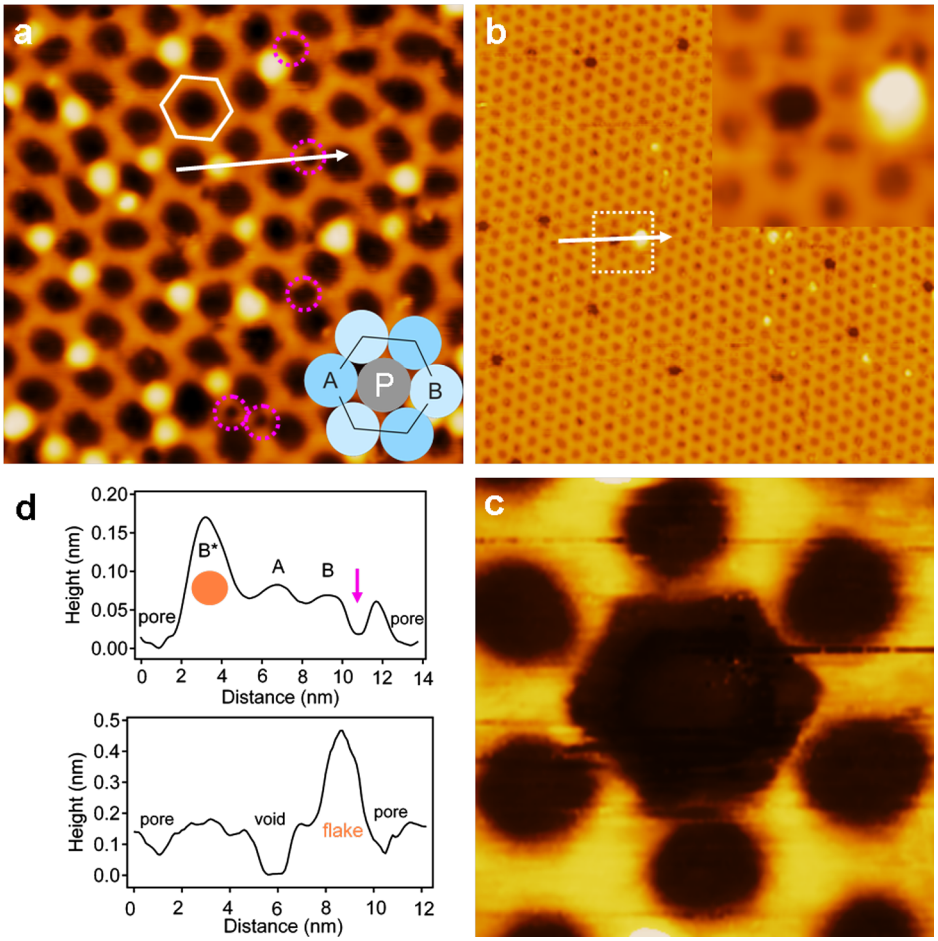

Figure 1. Ar nanotent formation and "can-opener" effect. (a) Room temperature (RT) STM image (27 × 27 nm^2) of ion-implanted Ar nanotents (bright protrusions) beneath *h*-BN monolayer on Rh(111). Ar locates at two sites beneath nanomesh wire crossings (A and B), but not in the pores (P). The hexagon represents the honeycomb super cell, also shown in the right-bottom inset, and the pink circles indicate vacancy defects generated by the Ar penetration. $U_t = -1.10$ V, $I_t = 0.10$ nA. (b) RT-STM image (90 × 90 nm^2) showing the "can-opener" effect after annealing of *h*-BN/Ar/Rh(111) to 900 K: Formation of 2 nm holes (voids) at pore sites. The bright flakes correspond to the 2 nm cut-outs. $U_t = -1.10$ V, $I_t = 0.10$ nA. The right-up inset is the zoom-in image of the white frame, showing a void and a flake. (c) High-resolution STM image displays the shape of a void after "can-opener" effect. 8.3 × 8.3 nm^2, $U_t = -1.00$ V, $I_t = 0.10$ nA. (d) Cross-sectional profiles along the white arrow in panel (a) and (b), which show the height difference of pore, occupied site, empty site, void and flake.

ratio between the two distinct sites is influenced by the ion dose and the annealing temperature.[29] Here, we elucidate the "can-opener" effect:[24] That is, how highly regular holes with 2 nm diameter (later on called voids) are cut upon an annealing process within a *h*-BN monolayer that was exposed to a given ion dose. These 2 nm voids within the *h*-BN layer are shown to be repulsive, and their density can be modified by the Ar ion dose prior to annealing. Finally, we present scanning tunneling microscopy (STM) data of the self-healing of the *h*-BN monolayer on a Rh(111) substrate: Annealing above 1000 K leads to the annihilation, *i.e.*, disappearance of the 2 nm voids that merge in larger holes in the *h*-BN layer. These results bring the fuctionlization of sp^2 layer systems a vital step forward and will eventually allow engineering of porous membranes for practical applications, such as DNA sequencing,[30] nanofiltration,[21] and water purification and desalination.[31]

RESULTS AND DISCUSSION

When pristine *h*-BN nanomesh is exposed to low energy Ar^+ ions, the ions penetrate the *h*-BN monolayer and accumulate above the Rh(111) surface to form the so-called "nanotent" structures,[24,29] as shown in Figure 1a. At room temperature the Ar nanotents appear as bright protrusions in the STM topography image. These nanotents have robust signatures, and can be observed at positive and negative tunneling voltages. They are stable at room temperature and also survive exposure to air. The implantation is a site-selective process: Ar atoms only immobilize beneath two distinct nanomesh wire-crossing sites (labeled as A and B), but not in the pores (P). The hexagon in Figure 1a represents the honeycomb super cell, also shown in the right-bottom inset. The ion bombardment sputters out boron and nitrogen atoms, leaving vacancy defects within the *h*-BN layer, as marked with pink circles in Figure 1a. Remarkably, after annealing

the *h*-BN/Ar/Rh(111) system to 900 K, the Ar nanotents disappear, and highly regular voids with 2 nm diameter form in the *h*-BN monolayer with adjacent flakes on the surface. At first sight it is surprising that the material in the pores, which is bound closer to the substrate,[20,32] detaches from the surface. However, this observation does nicely confirm that the main stability of the sp^2 layer is given by the in plane σ-bonds, while the strong adherence of the layer to the substrate, which is reflected in its stability up to 1160 K,[33] requires large area sp^2 islands. We assign the flakes near the 2 nm voids to the cut-out from the pore sites during the annealing process, similar to a "lid" cut from a tin can, which lead us to call the formation process "can-opener" effect[24] (see Figure 1b). The right-top inset, which is the zoom-in STM image of the white frame in the middle, illustrates one void and its corresponding flake. Figure 1c displays a high resolution STM image of a void after removing of a *h*-BN flake at a pore site. The shape of the 2 nm void clearly shows a hexagon here. Figure 1d displays the line profiles of the two white arrows in Figure 1a,b. The cut in Figure 1a runs across a nanotent at a B site, one empty A site, one empty B site, a vacancy defect generated by Ar implantation and a pore site. The cross-sectional profile in Figure 1b shows the height difference of pores, voids and flakes.

The ion bombardment causes not only population of Ar nanotents, but also generates vacancy defects, *i.e.*, knock out of boron or nitrogen atoms. Above room temperature, these vacancy defects become mobile. They may diffuse and assemble at the rim of the nanomesh pores, which leads to the "can-opener" effect, *i.e.*, the cut-out of the 2 nm "lids" (*h*-BN flakes) from the *h*-BN nanomesh pores. Density functional theory (DFT) predicts boron and nitrogen vacancies to assemble as BN vacancies in the pores. These pair defects, in turn, segregate to the rims of the pores, where the can-opener effect is enabled by further condensation of defects. At 900 K, the cut-out *h*-BN flakes are no longer bound to the *h*-BN layer *via* the strong σ-bonds, and also have relatively weak bonding to the Rh substrate. Therefore, they diffuse away from their origins. After trying different annealing temperatures, we found that the "can-opener" effect takes place in a rather broad temperature range between 700 and 1000 K. When the temperature approaches 1000 K, the regular 2 nm voids are still stable and can be observed by STM at room temperature, while the cut-out flakes disappear from the surface. This cutting temperature range is below the *h*-BN/Rh(111) decomposition temperature of 1160 K.[33] Accordingly, no "can-opener" effect is observed for samples that are annealed to the same temperature range without previous ion exposure. This confirms that the active species are introduced by ion implantation.

The STM image in Figure 1b illustrates that 2% of the nanomesh pores map as dark 2 nm voids in the *h*-BN layer, after an ion exposure of 380 nC/cm^2 that leads to a nanotent coverage of 3.6×10^{12} *protrusions*/cm^2 (0.321 protrusions/unit cell). This provides a key to the understanding of the "can-opener" effect that comprises the question on where the energy comes from in order to break about 62 BN-bonds. This number corresponds to an energy of about 400 eV, taking as BN bond energy 6.3 eV.[27] Here, we propose that this energy is paid by the impinging ions during the creation of vacancy defects, and that the energy remains stored until the defects start to agglomerate. In order to substantiate this picture, we performed DFT calculations of defects at different sites within the *h*-BN superhoneycomb. The results are summarized in Figure 2 and Table 1. All calculated vacancies on the *h*-BN nanomesh have a lower energy than the corresponding defect on free-standing *h*-BN. This is due to the fact that the substrate may partly compensate the dangling bonds that are created upon the removal of boron or nitrogen from *h*-BN. Single boron or nitrogen vacancies are most stable in the center of the nanomesh pores, and least stable on the wires. This is rationalized by the fact that besides the dominant bond-energy in the BN σ-bonds, the bond-energy to the rhodium substrate is strongest in the pores.[32] Table 1 also clearly shows that the nitrogens are bonding stronger to the rhodium substrate.[27] If single vacancy defects start to diffuse they are therefore expected to be trapped in the pores. Furthermore, a nitrogen and a boron vacancy are expected to associate and to form BN vacancies, since this lowers the total energy of the defects. This is mainly due to the reduction of the number of broken BN bonds. Such single vacancy association must be particularly efficient, because the vacancies are trapped in the 2 nm pores and remain trapped after association. Importantly, the calculations indicate a BN pair-vacancy with a 50 meV lower energy at the rim of the pore (BN = 33) (see Figure 2), which makes the rims attractive for BN vacancies. Since the rim is a one-dimensional ring-object, it must be particularly efficient to merge there. Such that the double vacancies finally become so abundant at a rim and induce the "can-opener" effect.

Given this "can-opener" scenario, it becomes clear on how decisive the nanomesh structure is in order to allow for such an unexpected effect: Without the subtle site dependence of the vacancy energies within the unit cell, it can not be explained why 2 nm voids are formed in a kind of self-assembly process, since the minimization of dangling bonds would simply lead to vacancy diffusion to the edge of the *h*-BN layer.

To further investigate the void *versus* nanotent coverage, a series of measurements have been carried out with cycles of Ar implantation and subsequent annealing, which can lead to an accumulation of voids. The relation between the void-coverage (Θ_{void}, number per nanomesh unit cell) and the Ar nanotent-coverage (Θ_{tent}, number per unit cell) is displayed in

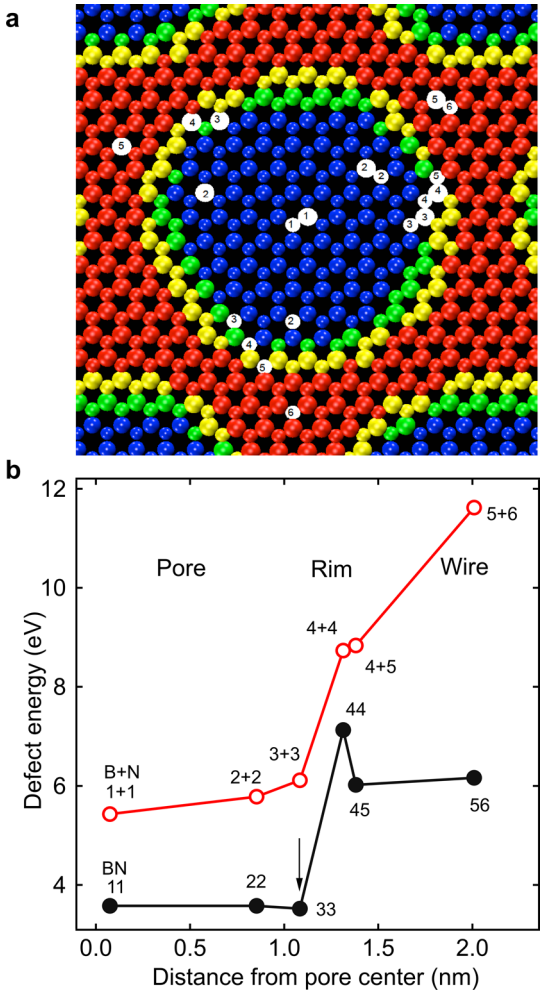

Figure 2. Single B, N and double BN vacancies in *h*-BN nanomesh. (a) Top view of the *h*-BN nanomesh. The color coding of the atoms reflects the height above the substrate. The blue atoms belong to the pores ($h < 2.4$ Å), green ($2.4 < h < 2.9$ Å) and yellow ($2.9 < h < 3.6$ Å) to the rim, red to the wires ($h > 3.6$ Å). The calculated defects are marked as white disks (large for boron, smaller for nitrogen) and labeled with numbers used in Table 1. The B, N and BN defects are distributed on 3 symmetry equivalent radii. (b) Defect energies of B+N (red) and BN (black) as a function of their distance from the pore center. The single defects have lowest energy in the pore, while the 33 BN defects at the rim (black arrow) have 50 meV lower energy than 11 in the center of the pore. This indicates defect trapping and provides theoretical support for the "can-opener" effect.

Figure 3a. Clearly, Θ_{void} increases with the Θ_{tent}, and it can be tuned by the number of Ar nanotents, until a too high Ar exposure destroys the nanomesh structure. The fitting line reveals the probability for the "can-opener" effect, *i.e.*, the number of voids with the accumulated number of nanotents prior to annealing. The initial slope of the Θ_{void} *vs* Θ_{tent} curve is 5.1%, which indicates that about 20 tents lead to one void. The fact that at room temperature Ar nanotents harbor more than one Ar atom[29] implies that one nanotent leaves more than one vacancy defect. That is, there is enough energy in the vacancy defects for the creation of the voids.

TABLE 1. Calculated Formation Energies in eV of Single Boron or Nitrogen and Double Boron Nitride (BN) Vacancy Defects in Freestanding *h*-BN and in the *h*-BN/Rh(111) Nanomesh, Where the Location of the Defect Is Given As a Distance from the Pore Center (See Figure 2)

label	energy (eV)	distance (nm)
boron		
h-BN	7.801	—
1	1.838	0.148
2	2.220	0.820
3	2.591	1.148
4	5.192	1.374
5	5.227	2.081
nitrogen		
h-BN	7.952	—
1	3.594	0.000
2	3.563	0.883
3	3.524	1.017
4	3.543	1.252
5	3.644	1.385
6	6.394	1.939
BN		
h-BN	8.547	—
11	3.577	0.074
22	3.578	0.853
33	3.523	1.083
44	7.130	1.313
45	6.023	1.380
56	6.166	2.009

The color coding of the data in Figure 3a indicates different preparation protocols: The red squares reflect a series where the voids were accumulated in repeated ion exposure/900 K annealing cycles, while the green squares represent a series with ion exposure/900 K annealing/1050 K annealing cycles that leads to the annihilation of the voids at the end of every cycle. To date we did not succeed to create void-coverages above 5% and take this as an indication for the repulsive interaction between the voids (see below).

Figure 3b–g shows the red series on the same *h*-BN/Rh(111) sample at different locations, since it is extremely difficult to find a given area on the sample after annealing that imposes the move of the sample from analysis position to the heating stage. Images of three subsequent cycles of ion exposure and annealing to 900 K are shown. The initial surface is exposed to low energy Ar^+ ions corresponding to a sputter charge density of 66 nC/cm^2, which generates 0.055 protrusions/unit cell. Figure 3c shows a void-coverage of 0.003 per unit cell after annealing to 900 K. Subsequently, the same sample is exposed to Ar ions with a sputter charge density of 250 nC/cm^2 (Figure 3b). The large-area STM image in Figure 3d displays an Ar nanotent-coverage of 0.199 protrusions/unit cell. Remarkably, the existing 2 nm voids on the surface do not influence significantly further Ar^+ ion exposure. Ar atoms are still located underneath the wire-crossings of the nanomesh and no Ar atoms can be observed

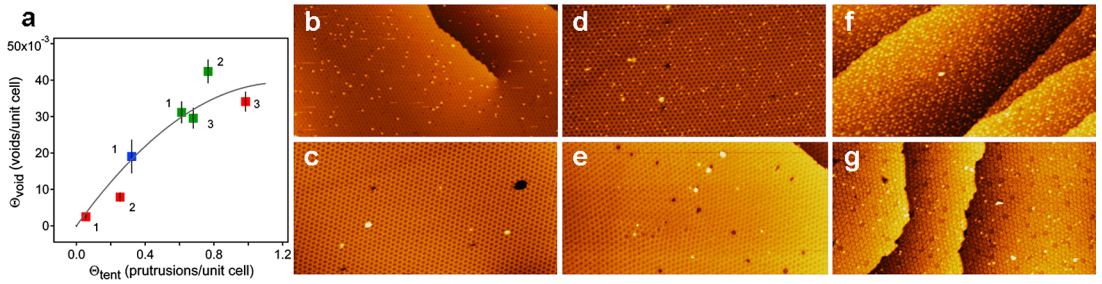

Figure 3. Void *versus* tent coverage dependence. (a) Void-coverage Θ_{void} (number/nanomesh unit cell) *versus* Ar nanotent-coverage Θ_{tent} (number/unit cell). The initial slope indicates that about 20 nanotents yield one void and no void-coverage above 5% could be prepared. The red color displays a series where the voids were accumulated in repeated ion exposure/900 K annealing/1050 K annealing cycles, while the green squares represent a series with ion exposure/900−1050 K annealing cycles, and the blue square shows one cycle of ion dose/900 K annealing treatment. The nanotent coverages for the red series are the first ion dose (1), the sum of the first + second ion doses (2) and the first + second + third ion doses (3). The numbers 1, 2 and 3 indicate the sequence of the applied cycles of ion dose and subsequent annealing. (b−g) Room temperature STM data of void-coverage-tuning for the same sample correspond to the red data series in (a). Annealing temperatures are 900 K. 190 × 95 nm^2, $U_t = -1.10$ V, $I_t = 0.50$ nA. (b,c), (d,e) and (f,g) are STM images of three subsequent cycles of ion dose and annealing. (b) *h*-BN nanomesh was exposed to Ar ions (0.055 protrusions/unit cell) and generated voids coverage of 0.003/unit cell in (c) after annealing. (d) The sample was exposed to Ar ions again, which shows 0.199 Ar protrusions/unit cell. (e) Voids coverage of 0.010/unit cell after annealing (d). (f) The third time of ion dose indicates 0.730 protrusions/unit cell. (g) High coverage of 2 nm voids of 0.045/unit cell after annealing (f).

inside of the pores and voids. This supports that most of the *h*-BN monolayer survives the low ion doses. After the second annealing, the 2 nm void coverage increases to 0.010 per unit cell (Figure 3e). Figure 3f displays the sample status after exposing the sample in Figure 3e to 860 *nC*/cm^2 of Ar^+ ions, which shows Ar nanotent-coverage of 0.730 protrusions/unit cell. After the third annealing treatment, Figure 3g shows increased void coverage of 0.045 per unit cell. Attempts to increase the void coverage Θ_{void} beyond 5% with more cycles of ion exposure and subsequent annealing failed, the Θ_{void} tends to saturate, and can not be further increased.

If we take a closer look to the distribution of the voids on the surface, it is noticed that it is not random, as it would be expected if there is no interaction between the voids. Figure 4a is a room temperature STM image of *h*-BN nanomesh with two steps (descending from left to right) and a void-coverage Θ_{void} of 5% per nanomesh unit cell. All voids are marked with circles, while different colors represent the different terraces (red, green and blue). The histogram in Figure 4b displays the distribution of the 2 nm voids as a function of the distance from the steps. The distance to the steps is marked with positive or negative values indicating the lower or upper terrace of the step, respectively. The distance 0 represents the location of the steps. Clearly, it shows that the voids prefer to locate along the steps, but on the lower terrace. We do not expect that the primary ion impact is strongly influenced by the steps, and therefore a random distribution of vacancy defects is expected, as it was observed for the nanotent distribution.[24] This indicates that there must be an attractive interaction to the lower bounds of steps for the vacancy defects and/or the voids. On the basis of the results in Table 1, single and double vacancies like to reside in the pores, where they are trapped. We thus propose the void-density variation to be due to void-mobility, attractive and repulsive interactions of the voids to the lower and the higher level of a step, respectively. This is reminiscent to the well-known attractive interaction between monatomic steps and molecules, although the nature of the interactions might have different origins. For instance, the strain field that is induced by the rim of the voids, where the remaining dangling bonds partly saturate with BN bonding to the underlying rhodium substrate.

Nonrandom distribution of the voids is also reflected in Figure 4c that shows a large-area STM image (175 × 175 nm^2) of *h*-BN monolayer with 2 nm void-coverage of 3% per nanomesh unit cell at room temperature. The statistics of the distances between these voids (pair correlation) is shown in the histogram in Figure 4d. The red line in the histogram represents the expectation of a random distribution, where the zero-probability for void−void distances below the nanomesh lattice constant of 3.2 nm indicates that two voids may not be superimposed. Apparently, a random distribution does not apply for the voids. The absence of void−void distances below 8 nm suggests that the interactions between voids are repulsive. This statement does not account for double voids that are about an order of magnitude less abundant than the 2 nm single voids. Double voids are surrounded by 9 instead of 6 intact pores as it is the case for single voids (see Figure 1). The existence of a maximum void-coverage (5%), as discussed above, is also consistent with repulsive interaction. Such void−void repulsion may have origins, such as the strain field due to the saturation of the dangling bonds and/or possible electrostatic dipole interactions between the voids.

Like the single vacancies, the voids may also diffuse, though at a higher temperature. Indeed, heating an ion

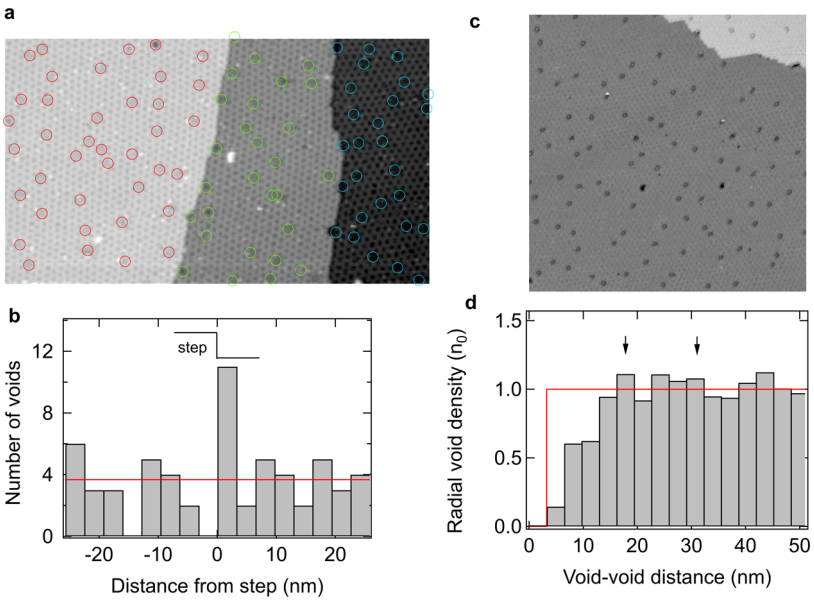

Figure 4. Nonrandom void distributions. (a) STM image of *h*-BN nanomesh with two steps and a void-coverage Θ_{void} = 5%. The voids are marked with different colors on different terraces. 182 × 104 nm^2 $U_t = -1.10$ V, $I_t = 0.10$ nA. (b) Void-distribution in (a) *versus* closest distance to the step. Negative and positive distances are measured on the top and bottom terraces, respectively. The voids favor to assemble at the lower side of the steps. (c) Large-area STM image (175 × 175 nm^2) of *h*-BN nanomesh after the "can-opener" effect, with a void-coverage Θ_{void} of 0.03/unit cell. Two of the voids near the center of the image map darker and are identified as double voids. $U_t = -1.20$ V, $I_t = 0.50$ nA. (d) Radial density of the void−void distances (pair correlation) in (c). The red line is the expectation for a random distribution. The deviation of the experiment from the red line can be explained with repulsive interaction of the voids. The arrows indicate the expected nearest and second nearest neighbor distances for a hexagonal supersuper structure with a density Θ_{void} of 3%.

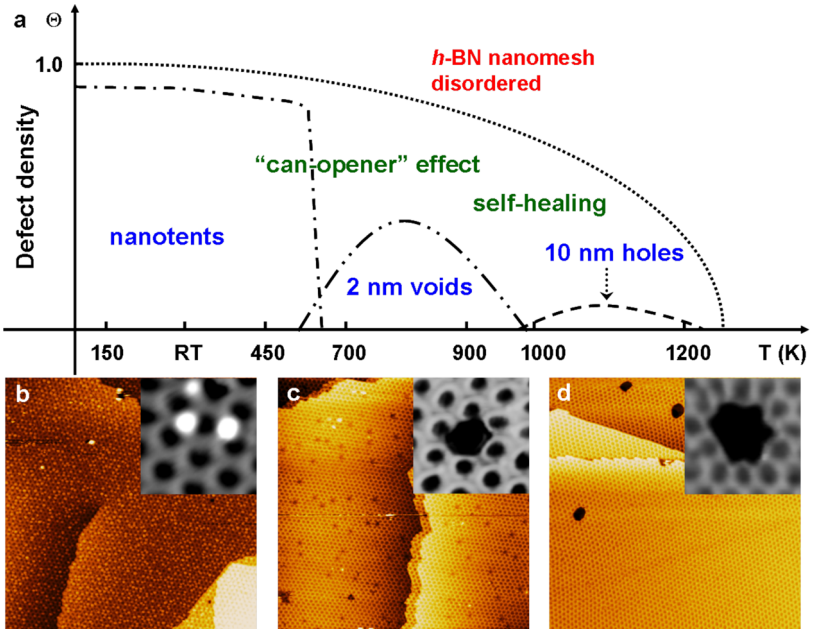

Figure 5. "Phase" diagram of the *h*-BN/Ar/Rh(111) nanomesh. (a) The temperature-dependent "phase" diagram of *h*-BN monolayer. When the nanotent coverage (Θ) is smaller than 1 protrusion/unit cell, three distinct temperature zones can be defined: Nanotent formation and Ar clustering (T < 650 K), "can-opener" effect induces 2 nm voids (700−960 K) and self-healing leads to 10 nm holes formation (1000−1200 K). If Θ > 1 or T > 1250 K, the superstructure of *h*-BN nanomesh is disordered or destroyed. (b−d) Large-size RT-STM images (190 × 190 nm^2) display the three different "phase" status of the same sample: Nanotent formation, 2 nm voids and 10 nm holes within *h*-BN monolayer, respectively. The three insets are the corresponding zoom-in STM images. (b) $U_t = -1.20$ V, $I_t = 0.50$ nA; (c) $U_t = -1.00$ V, $I_t = 0.50$ nA; (d) $U_t = -1.50$ V, $I_t = 0.50$ nA. The big empty holes are formed after annealing above 1000 K.

exposed *h*-BN/Rh(111) sample with voids to a temperature higher than 1000 K, where the "can-opener" effect took place (Figure 5c), a further phenomenon is observed: The voids disappear and larger holes

(bigger than 10 nm) form on the surface. As a consequence the surface recovers as intact *h*-BN monolayer and this "self-healing" just leaves some large empty holes, as shown in Figure 5d. It is worth to note that pristine *h*-BN nanomesh may also contain large holes prior to any treatment.[5] Their formation might due to the migration of residual defects during the growth that minimize the total energy cost. This offers an argument on why overall *h*-BN/Rh(111) forms an almost perfect, two-dimensional crystal. However, the number and the size of the large holes significantly increases after ion irradiation and high temperature treatment close to the synthesis temperature of the *h*-BN nanomesh, at which the self-healing of the nanomesh occurs. At high temperature, the voids migrate to the edges of the big holes and annihilate in joining them, which minimizes the number of broken BN bonds. The "self-healing" effect allows the repeated use of *h*-BN monolayer for further functionalization. Self-healed *h*-BN nanomesh can be exposed to Ar ions again and the annealing procedure leading to voids (see green squares in Figure 3a). The "can-opener" effect creates 2 nm voids, which may coexist with the remaining large holes. A subsequent high temperature treatment leads to the "self-healing" of the *h*-BN again, which can be used as a nanotemplate once more. For instance, for further ion bombardment and annealing procedures. And so on, almost *ad infinitum*, as long as the temperature is below 1200 K, where the *h*-BN nanomesh starts to disintegrate.[33]

Figure 5a provides the present understanding of the different observed defects and their interplay in a kind of "phase" diagram of the *h*-BN/Ar/Rh(111) system. We use quotation marks for "phase" since it is clear from the above that we deal not with thermodynamic phases, but rather with kinetically stable phases. The two parameters in the diagram are the defect density (Θ_{defect}, number/unit cell) and the sample temperature (T, K). For the interval $0 < \Theta_{defect} < 1$, nanotents, *i.e.*, stable atomic agglomerates between the *h*-BN and the Rh substrate are observed. For $\Theta_{defect} > 1$, the *h*-BN monolayer is fully covered with nanotents, and the nanomesh superstructure is destroyed. If the sample temperature T gets higher than the critical temperature (1200 K), the *h*-BN monolayer starts disintegration, gets disordered and eventually disappears. Therefore, the focus has been put on the regions with conditions of $0 < \Theta_{defect} < 1$ and $T < 1200$ K. The "phase" diagram shows the three distinct morphologies or "phases" in three temperature windows: Nanotents $T < 700$ K (zone I), 2 nm voids 700 K $< T <$ 1000 K (zone II) and intact (self-healed) *h*-BN monolayer with holes larger than 10 nm 1000 K $< T <$ 1200 K (zone III). The "can-opener" effect shapes the sample in zone II, and the "self-healing" occurs in zone III. In temperature zone I, Ar is stabilized between *h*-BN and Rh substrates, under the wire-crossings (Figures 1a, 3b,d,f, and 5b). When T approaches zone II, Ar nanotents decrease in number while they grow in size upon temperature increase, which indicates Ar clustering.[29] More importantly, when T increases to 700 K, the vacancy defects become active, *i.e.*, start to diffuse, and they prefer to assemble below steps. Further raising of the temperature results in the self-healing of the *h*-BN monolayer, in which the 2 nm voids disappear and some larger holes emerge (Figure 5d). The processes within temperature below 1200 K are repeatable, and the coverage of the 2 nm voids and 10 nm holes can be well controlled within the given limits. Of course, the lines between the different temperature zones are not as sharp as in a first order phase transition. For instance, very few of 2 nm voids are observed after annealing to 650 K in temperature zone I. We also tried different annealing times for the same temperature. It turns out the time is not an as critical factor as it is the temperature for the whole process.

CONCLUSIONS

In conclusion, the creation and control of 2 nm voids within a single layer of the *h*-BN nanomesh honeycomb superstructure on a Rh substrate and the "self-healing" of such monolayer at high temperature are reported. The density of the highly regular voids can be tuned by the ion exposure up to a density of 5% of the nanomesh pores. These voids are repulsive and isolated, and they favor the lower level of atomic steps of the substrate. Systematic measurements reveal that the entire process, including nanotent formation, "can-opener" effect and nanomesh "self-healing", is well controlled and repeatable. The repeated generation of 2 nm voids and repeated use of the *h*-BN monolayer pave the way to the practical applications of *h*-BN monolayer, such as gasfiltration, desalination and water purification.

METHODS

Experimental Section. The experiments were performed in an ultrahigh vacuum (UHV) system with a base pressure of 1×10^{-10} mbar with a variable-temperature scanning tunneling microscope (Omicron VT-STM). The *h*-BN nanomesh samples were produced with the standard recipe.[5] The ion implantation was achieved with a Specs IQP 10/35 Penning-type ion source run at lowest acceleration potential. The sputter charge density corresponds to the integrated sputter current density. The STM measurements were carried out with electrochemically etched tungsten tips. All STM images were taken in constant-current mode.

Theory. Calculations are performed using Kohn–Sham DFT within the GPW formalism as implemented in the Quickstep module in the CP2K program package.[34] Dual-space pseudopotentials[35] are used to describe the interaction of valence

electrons with atomic cores. The pseudopotentials for boron and nitrogen assume 3 and 5 valence electrons, respectively. The atomic cores of the Rh are described by potentials with 9 valence electrons. The Gaussian basis sets chosen for this type of application are of the molecularly optimized type.[36] The PW energy cutoff for the expansion of the density is set at 500 Ry. The Brillouin zone is sampled only at the Γ point. Exchange and correlation are calculated with the Perdew–Burke–Ernzerhof (PBE)[37] GGA exchange-correlation (XC) functional. Long-range dispersion interactions have been computed using DFT-D3 formalisms.[38]

We employ a slab-like model where the simulation cell consists of four layers of 12 × 12 Rh(111) units terminated on one side by a 13 × 13 *h*-BN overlayer. Periodic boundary conditions are applied, and interactions with periodic images in the direction perpendicular to the exposed surface are avoided by adding about 20 Å of vacuum space above the slab. The atoms at the bottom Rh layer are kept fixed in the bulk positions. This computational setup has been already successfully applied for several previous studies related to *h*-BN/Rh(111).[27,39] In particular, the combination of PBE functional and D3 Grimme correction reproduce the pore/wire shape and proportions with the best agreement with high atomic resolution STM images, so far.[40]

Each vacancy defect has been generated by removing the corresponding atoms from the optimized nanomesh structure. After the complete relaxation of the defective system, the vacancy formation energy is obtained in terms of the chemical potentials of the atomic species μ_B and μ_N, as

$$E_f = E_{dnm} - E_{nm} + n_{vN}\mu_N + n_{vB}\mu_B$$

where the number of removed B and N atoms per nanomesh unit cell are n_{vB} and n_{vN}, respectively, while E_{nm} and E_{dnm} are the total energies of pristine and defective nanomesh. The reference chemical potentials of B and N are determined under the constraint $\mu_{BN} = \mu_B + \mu_N$, where μ_{BN} is the pair energy computed for free-standing *h*-BN and μ_N is obtained from gas phase N_2.[41]

Conflict of Interest: The authors declare no competing financial interest.

Acknowledgment. Financial support by the Swiss National Science Foundation and support by the EC under the Graphene Flagship (Contract No. CNECT-ICT-604391) is gratefully acknowledged. We thank the Swiss National Supercomputer Centre (CSCS) for the generous allocation of computer time.

REFERENCES AND NOTES

1. Batzill, M. The Surface Science of Graphene: Metal Interfaces, CVD Synthesis, Nanoribbons, Chemical Modifications, and Defects. *Surf. Sci. Rep.* **2012**, *67*, 83–115.
2. Pakdel, A.; Bando, Y.; Golberg, D. Nano Boron Nitride Flatland. *Chem. Soc. Rev.* **2014**, *43*, 934–959.
3. Geim, A. K.; Novoselov, K. S. The Rise of Graphene. *Nat. Mater.* **2007**, *6*, 183–191.
4. Song, L.; Ci, L.; Lu, H.; Sorokin, P. B.; Jin, C.; Ni, J.; Kvashnin, A. G.; Kvashnin, D. G.; Lou, J.; Yakobson, B. I.; Ajayan, P. M. Large Scale Growth and Characterization of Atomic Hexagonal Boron Nitride Layers. *Nano Lett.* **2010**, *10*, 3209–3215.
5. Corso, M.; Auwärter, W.; Muntwiler, M.; Tamai, A.; Greber, T.; Osterwalder, J. Boron Nitride Nanomesh. *Science* **2004**, *303*, 217–220.
6. N'Diaye, A. T.; Bleikamp, S.; Feibelman, P. J.; Michely, T. Two-Dimensional Ir Cluster Lattice on a Graphene Moire on Ir(111). *Phys. Rev. Lett.* **2006**, *97*, 215501.
7. Sutter, P. W.; Flege, J.-I.; Sutter, E. A. Epitaxial Graphene on Ruthenium. *Nat. Mater.* **2008**, *7*, 406–411.
8. Sutter, P.; T, S. J.; Sutter, E. Graphene on Pt(111): Growth and Substrate Interaction. *Phys. Rev. B: Condens. Matter Mater. Phys.* **2009**, *80*, 245411.
9. Brugger, T.; Günther, S.; Wang, B.; Dil, J. H.; Bocquet, M.-L.; Osterwalder, J.; Wintterlin, J.; Greber, T. Comparison of Electronic Structure and Template Function of Single-Layer Graphene and a Hexagonal Boron Nitride Nanomesh on Ru(0001). *Phys. Rev. B: Condens. Matter Mater. Phys.* **2009**, *79*, 045407.
10. Li, X. S.; Cai, W. W.; An, J.; Kim, S.; Nah, J.; Yang, D. X.; Piner, R.; Velamakanni, A.; Jung, I.; Tutuc, E.; Banerjee, S. K.; Colombo, L.; Ruoff, R. S. Large-Area Synthesis of High-Quality and Uniform Graphene Films on Copper Foils. *Science* **2009**, *324*, 1312–1314.
11. Coletti, C.; Riedl, C.; Lee, D. S.; Krauss, B.; Patthey, L.; Klitzing, K.; Smet, J. H.; Starke1, U. Charge Neutrality and Band-Gap Tuning of Epitaxial Graphene on SiC by Molecular Doping. *Phys. Rev. B: Condens. Matter Mater. Phys.* **2010**, *81*, 235401.
12. Joshi, S.; Ecija, D.; Koitz, R.; Iannuzzi, M.; Seitsonen, A. P.; Hutter, J.; Sachdev, R.; Vijayaraghavan, S.; Bischoff, F.; Seufert, K.; Barth, J. V.; Auwärter, W. Boron Nitride on Cu(111): An Electronically Corrugated Monolayer. *Nano Lett.* **2012**, *12*, 5821–5828.
13. Dil, H.; Lobo-Checa, J.; Laskowski, R.; Blaha, P.; Berner, S.; Osterwalder, J.; Greber, T. Surface Trapping of Atoms and Molecules with Dipole Rings. *Science* **2008**, *319*, 1824–1826.
14. Ma, H. F.; Ding, Y.; Iannuzzi, M.; Brugger, T.; Berner, S.; Hutter, J.; Osterwalder, J.; Greber, T. Chiral Distortion of Confined Ice Oligomers (*n* = 5,6). *Langmuir* **2012**, *28*, 15246–15250.
15. Tseng, T.; Urban, C.; Wang, Y.; Otero, R.; Tait, S. L.; AlcamAś, M.; Écija, D.; Trelka, M.; Gallego, J. M.; Lin, N.; Konuma, M.; Starke, U.; Nefedov, A.; Langner, A.; Wöll, C.; *et al.* Charge-Transfer-Induced Structural Rearrangements at both Sides of Organic/Metal Interfaces. *Nat. Chem.* **2010**, *2*, 374–379.
16. Auwärter, W.; Muntwiler, M.; Greber, T.; Osterwalder, J. Co on *h*-BN/Ni(111): from Island to Island-Chain Formation and Co Intercalation. *Surf. Sci.* **2002**, *511*, 379–386.
17. Preobrajenski, A. B.; Ng, M. L.; Vinogradov, N. A.; Vinogradov, A. S.; Lundgren, E.; Mikkelsen, A.; Martensson, N. Impact of Oxygen Coadsorption on Intercalation of Cobalt under the *h*-BN Nanomesh. *Nano Lett.* **2009**, *9*, 2780–2787.
18. Brugger, T.; Ma, H.; Iannuzzi, M.; Berner, S.; Winkler, A.; Hutter, J.; Osterwalder, J.; Greber, T. Nanotexture Switching of Single-Layer Hexagonal Boron Nitride on Rhodium by Intercalation of Hydrogen Atoms. *Angew. Chem., Int. Ed.* **2010**, *49*, 6120–6124.
19. Mao, J. H.; Huang, L.; Pan, Y.; Gao, M.; He, J. F.; Zhou, H. T.; Guo, H. M.; Tian, Y.; Zou, Q.; Zhang, L. Z.; Zhang, H. G.; Wang, Y. L.; Du, S. X.; Zhou, X. J.; Castro Neto, A. H.; *et al.* Silicon Layer Intercalation of Centimeter-Scale, Epitaxially Grown Monolayer Graphene on Ru(0001). *Appl. Phys. Lett.* **2012**, *100*, 093101.
20. Berner, S.; Corso, M.; Widmer, R.; Groening, O.; Laskowski, R.; Blaha, P.; Schwarz, K.; Goriachko, A.; Over, H.; Gsell, S.; Schreck, M.; Sachdev, H.; Greber, T.; Osterwalder, J. Boron Nitride Nanomesh: Functionality from a Corrugated Monolayer. *Angew. Chem., Int. Ed.* **2007**, *46*, 5115–5119.
21. O'Hern, S. C.; Boutilier, M. S. H.; Idrobo, J.-C.; Song, Y.; Kong, J.; Laoui, T.; Atieh, M.; Karnik, R. Selective Ionic Transport through Tunable Subnanometer Pores in Single-Layer Graphene Membranes. *Nano Lett.* **2014**, *14*, 1234–1241.
22. Ugeda, M. M.; Brihuega, I.; Guinea, F.; Gómez-Rodríguez, J. M. Missing Atom as a Source of Carbon Magnetism. *Phys. Rev. Lett.* **2010**, *104*, 096804.
23. Ugeda, M. M.; Fernández-Torre, D.; Brihuega, I.; Pou, P.; Martínez-Galera, A. J.; Pérez, R.; Gómez-Rodríguez, J. M. Point Defects on Graphene on Metals. *Phys. Rev. Lett.* **2011**, *107*, 116803.
24. Cun, H. Y.; Iannuzzi, M.; Hemmi, A.; Roth, S.; Osterwalder, J.; Greber, T. Immobilizing Individual Atoms beneath a Corrugated Single Layer of Boron Nitride. *Nano Lett.* **2013**, *13*, 2098–2103.
25. Standop, S.; Lehtinen, O.; Herbig, C.; Lewes-Malandrakis, G.; Craes, F.; Kotakoski, J.; Michely, T.; Krasheninnikov, A.; Busse, C. Ion Impacts on Graphene/Ir(111): Interface Channeling, Vacancy Funnels, and a Nanomesh. *Nano Lett.* **2013**, *13*, 1948–1955.
26. Å hlgren, E. H.; Hämäläinen, S. K.; Lehtinen, O.; Liljeroth, P.; Kotakoski, J. Structural Manipulation of the Graphene/Metal Interface with Ar^+ Irradiation. *Phys. Rev. B: Condens. Matter Mater. Phys.* **2013**, *88*, 155419.

27. Díaz, J. G.; Ding, Y.; Koitz, R.; Seitsonen, A. P.; Iannuzzi, M.; Hutter, J. Hexagonal Boron Nitride on Transition Metal Surfaces. *Theor. Chem. Acc.* **2013**, *132*, 1350–1366.
28. De Lima, L. H.; Cun, H. Y.; Hemmi, A.; Kaelin, T.; Greber, T. Note: An Ion Source for Alkali Metal Implantation beneath Graphene and Hexagonal Boron Nitride Monolayers on Transition Metals. *Rev. Sci. Instrum.* **2013**, *84*, 126104.
29. Cun, H. Y.; Iannuzzi, M.; Hemmi, A.; Osterwalder, J.; Greber, T. Implantation Length and Thermal Stability of Interstitial Ar Atoms in Boron Nitride Nanotents. *ACS Nano* **2014**, *8*, 1014–1021.
30. Zhou, Z.; Hu, Y.; Wang, H.; Xu, Z.; Wang, W. L.; Bai, X. D.; Shan, X. Y.; Lu, X. H. DNA Translocation through Hydrophilic Nanopore in Hexagonal Boron Nitride. *Sci. Rep.* **2013**, *3*, 3287.
31. Siria, A.; Poncharal, P.; Biance, A.; Fulcrand, R.; Blase, X.; Purcell, S. T.; Bocquet, L. Giant Osmotic Energy Conversion Measured in a Single Transmembrane Boron Nitride Nanotube. *Nature* **2013**, *494*, 455–458.
32. Laskowski, R.; Blaha, P. Unraveling the Structure of the *h*-BN/Rh(111) Nanomesh with *Ab Initio* Calculations. *J. Phys.: Condens. Matter.* **2008**, *20*, 064207.
33. Dong, G.; Fourre, E. B.; Tabak, F. C.; Frenken, J. W. M. How Boron Nitride Forms a Regular Nanomesh on Rh(111). *Phys. Rev. Lett.* **2010**, *104*, 096102.
34. CP2k Developers Group under the Terms of the GNU General Public Licence; see http://www.cp2k.org. 2012.
35. Goedecker, S.; Teter, M.; Hutter, J. Separable Dual-Space Gaussian Pseudopotentials. *Phys. Rev. B: Condens. Matter Mater. Phys.* **1996**, *54*, 1703–1710.
36. VandeVondele, J.; Hutter, J. Gaussian Basis Sets for Accurate Calculations on Molecular Systems in Gas and Condensed Phases. *J. Chem. Phys.* **2007**, *127*, 114105.
37. Perdew, J. P.; Burke, K.; Ernzerhof, M. Generalized Gradient Approximation Made Simple. *Phys. Rev. Lett.* **1996**, *77*, 3865–3868.
38. Grimme, S.; Antony, J.; Ehrlich, S.; Krieg, H. A Consistent and Accurate *Ab Initio* Parametrization of Density Functional Dispersion Correction (DFT-D) for the 94 Elements H-Pu. *J. Chem. Phys.* **2010**, *132*, 154104.
39. Ding, Y.; Iannuzzi, M.; Hutter, J. Investigation of Boron Nitride Nanomesh Interacting with Water. *J. Phys. Chem. C* **2011**, *115*, 13685–13692.
40. Iannuzzi, M.; Tran, F.; Widmer, R.; Dienel, T.; Radican, K.; Ding, Y.; Hutter, J.; Gröning, O. Site-Selective Adsorption of Phthalocyanine on *h*-BN/Rh(111) Nanomesh. *Phys. Chem. Chem. Phys.* **2014**, *16*, 12374–12384.
41. Okada, S. Atomic Configurations and Energetics of Vacancies in Hexagonal Boron Nitride: First-Principles Total-Energy Calculations. *Phys. Rev. B: Condens. Matter Mater. Phys.* **2009**, *80*, 161404.